

Astrometric CCD Observations of Titania and Oberon

A. Ogden

Durham University PHYS3601

Michaelmas Term 2020

Twelve CCD observations of Oberon and Titania are taken between October and November 2020. The images were calibrated using the Gaia catalogue and then compared to NASA's DE441 ephemeris. (O-C) residuals are presented and it is found that the observations are within $2''$ of the calculated data but that systematic errors may be present. The projection of the moon's orbits on the sky and their periodic behaviour over time are plotted. The periods of Oberon and Titania are determined as 13.470 ± 0.001 and 8.703 ± 0.001 days respectively.

I Introduction

In 1986, Voyager 2 became the first and last spacecraft to visit Uranus. Whilst its gas giant neighbours Jupiter and Saturn have since enjoyed dedicated missions Juno and Cassini; the ice giants Uranus and Neptune have not been so lucky and remain shrouded in relative mystery as a result. Perhaps the biggest mystery is their internal structure. Currently, it is thought that ice giants have a 3-layer structure: a dense, rocky core containing heavy elements, a thick layer of ice (a mixture of primarily water with other simple molecules like ammonia and methane) and an outer envelope of hydrogen and helium [1]. However, what little gravitational data we have from Voyager 2 suggests that this model is too simple [2]. In particular, both Uranus and Neptune are less condensed than this model suggests and that the heavier material may be partially distributed throughout the ice layer.

The mechanisms behind ice giant formation and evolution are also not fully understood [3]. Many models suggest that ice giants should be rare since there is a very narrow window in which they can form [4]. However, empirical data suggests that they are very common amongst exoplanets, even more abundant than gas giants [5]. This paradox is yet to be resolved. Additionally, these exoplanets share very few of Uranus and Neptune's properties like their large orbital radii [6]. This raises important questions about whether Uranus and Neptune are unique amongst ice giants. Sending a probe to orbit an ice giant is therefore of great scientific significance since it is the only way to gather the necessary data to answer these pressing questions and begin to fill in some of the biggest gaps in our understanding of planetary physics [7]. As such, many probe designs have already been proposed for launch around 2030 [8][9]. Successful probes orbit their planet for many years and regularly alter their orbits in order to gather a variety of data. This requires being able to predict the exact positions of all the bodies in a planetary system many years or decades into the future i.e. generating an ephemeris. This in turn motivates the determination of the orbital parameters of the moons around a planet with very high precision and accuracy from ground-based observations prior to the probe's launch.

CCD observations are frequently used to verify the ephemerides of the Uranian moons [10] [11] and are helpful in constraining and updating them when they lose accuracy [12]. A common method of performing astrometry on Solar System objects is to calibrate the CCD images using background reference stars which have known positions (from a star catalogue) [13]. A large



FIG. 1: True colour image of Uranus taken by the Voyager 2 spacecraft in 1986.[20]

field of view (FOV) is therefore advantageous since it means there will be a greater number of reference stars in the image. However, images of the Uranian system must have a small FOV (a few arcminutes) otherwise the much brighter planet will obscure the inner moons. Telescopes with long focal lengths have high enough resolutions at small FOVs to resolve the inner moons. If there happens to be a background star in the image, this can enable accurate astrometry of the moons [14]. Telescopes with a larger FOV that don't have the required resolution won't be able to resolve the inner moons; they are however able to calibrate images more reliably from background stars [15]. If by chance Uranus passes through a patch of sky with few stars, it can be difficult to calibrate using catalogues. One solution is the method of mutual approximations, where satellites are measured relative to each other rather than to background stars [16]. This has recently been applied to the Uranian system [17]. Until probe observations are made, the most precise astrometry comes from the method of mutual phenomena i.e. observing eclipses and occultations between moons. This commonly happens at Uranus' equinoxes every 42 years, since this is when Earth crosses the orbital plane of the system and is placed favourably to observe such phenomena. During Uranus' equinox in 2007 the moons were observed and their positions were determined to a high precision [18][19]. In this report, CCD images of Uranus are taken using small aperture telescopes and calibrated with known star catalogues. Astrometry of the two largest moons (Oberon and Titania) is performed and their positions are compared to an ephemeris. Their periods are recovered and compared to known values.

II Methods

A. Telescope

Images were taken using Durham University's Far East 16 and DRACO2 telescopes. Both are Meade LX200 telescopes. Details of the telescopes can be found in table I.

Parameter	Far East 16	DRACO2
Aperture (inches)	16	14
Focal Length (mm)	4064	3556
CCD size (pixels)	3326x2504	3326x2504
Image size after binning (pixels)	1110x835	1110x835
FOV (arcmin)	15.4x11.6	18.3x13.8
Image Scale (arcsec/pixel)	0.83	0.98

TABLE I: Details of telescopes used for observations. FOV and image scale are approximate values since they slightly vary between observations.

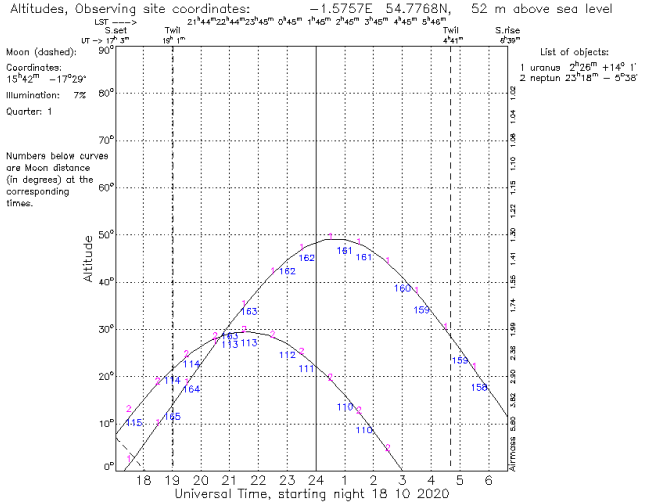
B. Target Selection

Uranus was selected over Neptune due to its better position in the sky during the observing period. Figure 2 shows that on 18th October 2020 Uranus reaches a maximum altitude of $\sim 50^\circ$ whereas Neptune only reaches $\sim 30^\circ$. The images of Uranus are therefore of higher quality since light travels through less air at higher altitudes and is affected less by atmospheric scattering. Additionally, Uranus was visible for a longer period each night since it spends more time above the minimum altitude reachable by the telescope.

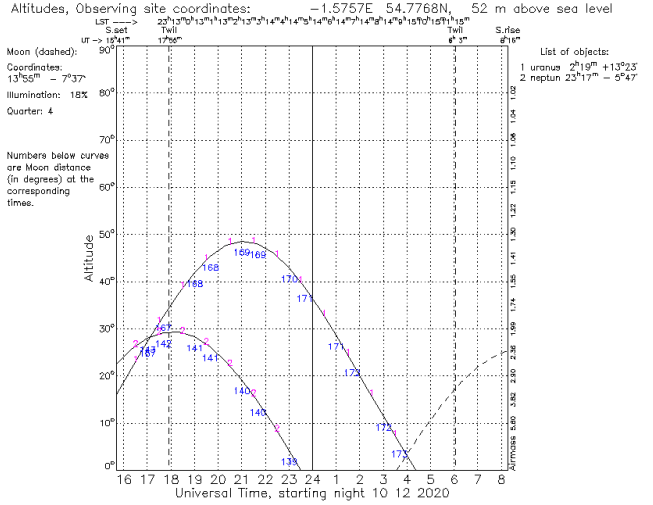
Uranus reaches its maximum altitude ~ 3 hours after Neptune. For example in figure 2 Uranus reaches its maximum altitude at 00:30 whereas Neptune does this at 21:30. Throughout the observing period, the planets will rise and set earlier each day. By mid-December, Neptune reaches its maximum altitude before twilight. It follows that Uranus' images will be darker and therefore less noisy than Neptune's, making it a better target. Uranus' moons were favourably orientated for CCD images during the observing period such that they were never obscured by each other or the planet at any point in their orbit as shown in figure 3.

C. Observations

A short exposure time is needed to resolve Uranus without the image being saturated, this is undesirable since it makes finding the centre of the planet more difficult. The moons are much fainter than Uranus due to their smaller size and lower albedo, so a long exposure time is needed to resolve them. Even when using the quickest exposure times which resolved the moons, Uranus still saturated the image. Since overexposure was unavoidable, the longest exposure time that did not include bleeding was chosen. The optimal exposure time changed between nights due to varying atmospheric and weather conditions. Every night, sample images were taken to determine the best exposure time for the current conditions. This can be seen in figure 4. The 15 s exposure has well defined moons but bleeding has occurred



(a) 18th October 2020



(a) 10th December 2020

FIG. 2: Altitude variations of Uranus and Neptune over one night as seen from Durham. Graphs generated using ING's STARALT program [21]. Co-ordinates of planets retrieved from JPL Horizons Web Interface [22].

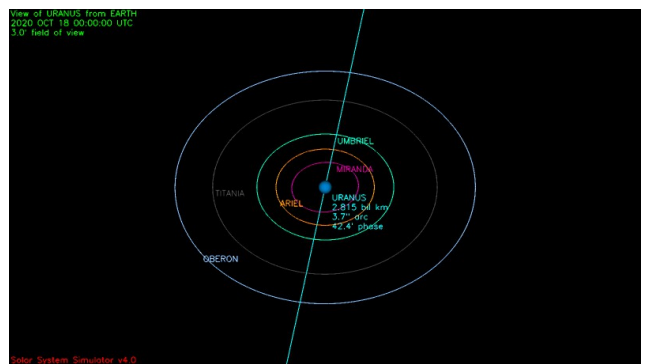


FIG. 3: 3 arcminute FOV simulated image of Uranus and its five major moons at midnight on the 18th October 2020 as seen on the sky. The orbits of the moons are shown as coloured rings and the names of the moons show their approximate positions. Image generated using JPL's Solar System Simulator [23].

around Uranus, whereas the moons are underexposed in the 1 s image. It was found that an exposure time of 4–8 s was best for a single image on a typical night.

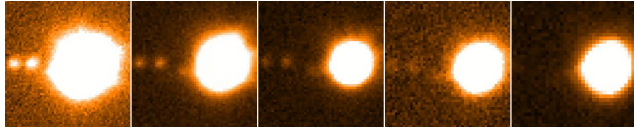


FIG. 4: Images of Uranus with varying exposure times. From left to right the exposure times are 15, 8, 4, 2 and 1 second(s) respectively. Images taken using DRACO2 on 15th October 2020.

The quality of the images was increased by stacking. By summing pixel values over many images and taking each pixel's median value, the signal to noise ratio (SNR) can be greatly increased as demonstrated in figure 5. This in turn increases the precision to which the positions of the moons can be determined. It was found that the sharpest images came from stacking many short exposure (1–4 s) images.

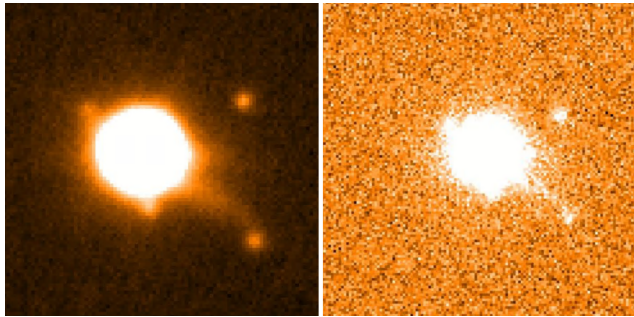


FIG. 5: A comparison between a 1 s exposure (right) and a stack of 64 1 s exposures (left). Images taken using Far East 16 on 5th November 2020. Both images are shown with a 99.5% scale limit.

Sample images were taken with a red filter and a clear filter. Since Uranus is more blue than the moons, it was thought that a red filter would disproportionately block light from the planet and make the moons relatively brighter. However, the red filter blocked too much light from the already faint moons so a clear filter was used for observations.

D. Image Processing

The positions of the moons were determined using the GAIA software's pick object function. Gaussian curves are fitted to each moon's brightness profile across one axis, the peak of this curve is then the position of the moon for the given axis (in pixels). This is repeated for both x and y axes in the image. The image is calibrated by finding background reference stars in the image and comparing them to their data in a catalogue of known stars. For this project, ESA's Gaia catalogue was used. This maps every pixel in the image to equatorial co-ordinates on the sky (in right ascension and declination). This also means the image scale (arcsec/pixel) can be precisely and uniquely calculated for each observation. This is important since, although each telescope has a fixed image scale, it can vary slightly between observations depending on the conditions and the altitude of objects being imaged.

The atmospheric scattering of the light from the moons

Date	Telescope	Exposure Time (s)	no. Images
01/10	D2	4	8
06/10	FE16	2	2
06/10	D2	4	4
08/10	D2	4	4
14/10	FE16	2	4
15/10	D2	4	4
22/10	D2	2	16
26/10	FE16	2	8
27/10	FE16	2	8
03/11	D2	1	64
05/11	FE16	1	64
10/11	D2	1	32

TABLE II: Details of observations, all dates in year 2020 and in format dd/mm. Telescopes DRACO2 and Far East 16 have been abbreviated as D2 and FE16 respectively

can be mathematically represented as a gaussian point spread function (PSF). When the image is well sampled (high SNR), the astrometric uncertainty in the position of the moons is equal to the uncertainty of this point spread function divided by SNR of that particular image [24]:

$$\sigma_{\text{AST}} = \frac{\sigma_{\text{PSF}}}{\text{SNR}} \quad (1)$$

Since the point spread function is Gaussian, the seeing (FWHM) conditions on the night can be related to the uncertainty by the known property $\sigma_{\text{PSF}} = \text{FWHM} \div 2.355$. By rewriting SNR as the ratio between mean counts (μ) and the error in mean counts (α), the astrometric error can be expressed as:

$$\sigma_{\text{AST}} = \frac{\text{FWHM } \alpha}{2.355 \mu} \quad (2)$$

The mean counts and error in mean counts of each moon is calculated using the GAIA software by drawing circular apertures around the moon and averaging the counts from each pixel. The same method cannot be used to find the centre of Uranus. Since Uranus always saturates the image, its brightness profile gets truncated at the pixel well depth and it has no peak. (since the CCD was 16 bit, the pixel well depth was $2^{16} = 65536$). Instead, the centre was determined using the circular shape of Uranus. If the image contained no bleeding, then the edge of the planet was well defined and approximated reasonably by a circle. Using the DS9 software, isophotal contours were drawn around the planet and smoothed until circular such that the centre of the isophotes was also the centre of Uranus. Repeating this process many times for the same image, using different isophote parameters each time, gave a set of planet positions. The final position of Uranus was recorded as the mean of these values.

MJD	Oberon		Observed		Calculated		O-C		Titania		Observed		Calculated		O-C	
	α_{rel}	δ_{rel}														
59123.97	-33.3	-7.5	-34.2	-7.3	0.9	-0.3			21.7	16.5	22.6	16.8	-0.8	-0.4		
59128.84	17.3	36.2	18.7	36.9	-1.4	-0.6			-25.2	-6.4	-25.5	-5.8	0.2	-0.6		
59128.86	18.1	35.9	19.0	36.7	-0.9	-0.8			-25.0	-6.0	-25.6	-5.3	0.6	-0.7		
59130.84	32.3	3.5	34.2	4.9	-1.9	-1.4			-6.9	29.2	-6.4	30.3	-0.4	-1.1		
59136.88	-31.3	-18.3	-32.0	-17.9	0.7	-0.4			-20.8	-19.9	-21.1	-19.6	0.3	-0.3		
59137.82	-34.2	0.9	-34.3	0.2	0.1	0.7			-25.6	0.5	-25.6	0.5	-0.0	-0.1		
59144.86	32.0	-6.5	33.3	-6.3	-1.3	-0.2			-10.9	-29.8	-11.0	-29.6	0.0	-0.3		
59148.99	-17.9	-37.5	-18.5	-37.3	0.5	-0.2			6.8	31.0	7.2	31.2	-0.4	-0.2		
59149.87	-27.8	-26.3	-28.3	-26.0	0.6	-0.3			19.3	20.7	20.3	21.1	-0.9	-0.4		
59156.80	28.3	22.4	29.7	22.9	-1.3	-0.5			-9.4	28.5	-9.0	29.1	-0.4	-0.6		
59158.91	28.8	-17.5	29.9	-17.4	-1.1	-0.1			22.3	14.4	23.3	14.7	-1.0	-0.3		
59163.98	-31.4	-14.9	-32.5	-14.8	1.0	-0.1			-24.6	1.3	-25.1	1.5	0.6	-0.3		

TABLE III: Comparison between the observed and calculated positions of moons relative to Uranus, units in arcseconds and rounded to 1 decimal place. Dates are in modified Julian days (MJD) rounded to 2 decimal places. O-C is the difference between observed and calculated positions.

To ensure all the images were orientated correctly (North up, East left) they were rotated by an angle (θ) which was calculated using the CD1_1 and CD2_1 WCS parameters in the header of the image FITS file:

$$\theta = 180^\circ - \arctan\left(\frac{\text{CD1_1}}{\text{CD2_1}}\right) \quad (3)$$

Images were transformed from pixels into arcseconds on the sky by multiplying the positions with the standard rotation matrix and the image scale (S):

$$\begin{pmatrix} x_{\text{arcsec}} \\ y_{\text{arcsec}} \end{pmatrix} = S \begin{pmatrix} x_{\text{pixels}} \\ y_{\text{pixels}} \end{pmatrix} \begin{pmatrix} \cos(\theta) & -\sin(\theta) \\ \sin(\theta) & \cos(\theta) \end{pmatrix} \quad (4)$$

Once the positions of the moons and Uranus were calculated and orientated correctly, the relative position on the sky of each moon with respect to Uranus could be determined.

III Results & Discussion

A. Astrometry

The astrometric data for the moon's relative positions to Uranus were compared with their calculated predicted positions in table III. The calculated positions were retrieved from JPL's DE441 ephemeris [25]. The observations appear to match the ephemeris well. No observation is more than $2''$ away from its calculated value and most are less than $1''$ away. However, the observations have uncertainties of $\sim 0.1''$, so in some cases they are many standard deviations (σ) away from their predicted value. This is visualised in figure 6. Across both moons and both right ascension and declination, the errors appear to be underestimated since many of the residuals have extremely large values of over 5σ . This is likely caused by finding the centre of Uranus using isophotes. The uncertainty in Uranus'

position came purely from the variance of the centres of different isophotes. Since the different isophotes were all drawn over the same stacked image, they all followed the same pixel count data and likely had very similar centres. The variance in these centres was very small and hence underestimated the errors. An alternative method would be to draw isophotes for every image in a stack. The centres of these isophotes should vary more since they are being drawn on separate images and hence get a more accurate error. This is very time consuming though, especially for the sharpest images with 64 frames in a stack. On top of that, this method is not a guaranteed improvement. Since the images are taken so close together, they may have very similar pixel values so the problem of similar contours may persist.

Another alternative would have been to take extremely short exposures, so Uranus did not saturate the image, in order to determine its centre using the same method as the moons' centres. If these short exposures were taken immediately before and after the moons were imaged with a stack of longer exposures, it would be reasonable to assume that Uranus' position calculated from the short exposures would be valid for the stack images. This method is not without problems. Firstly, Uranus is an extended source so if it was underexposed its true centre might not be accurately found by finding the peak of its brightness profile. Secondly, when the image is underexposed the SNR becomes very low and the image becomes dominated by photometric noise. This means that equation 1 cannot be used because the image is no longer background/sky noise limited since the signal noise has increased. The extent to which this affects the data is hard to predict since it depends on seeing conditions and the telescope parameters, however it may produce more realistic errors for Uranus' position.

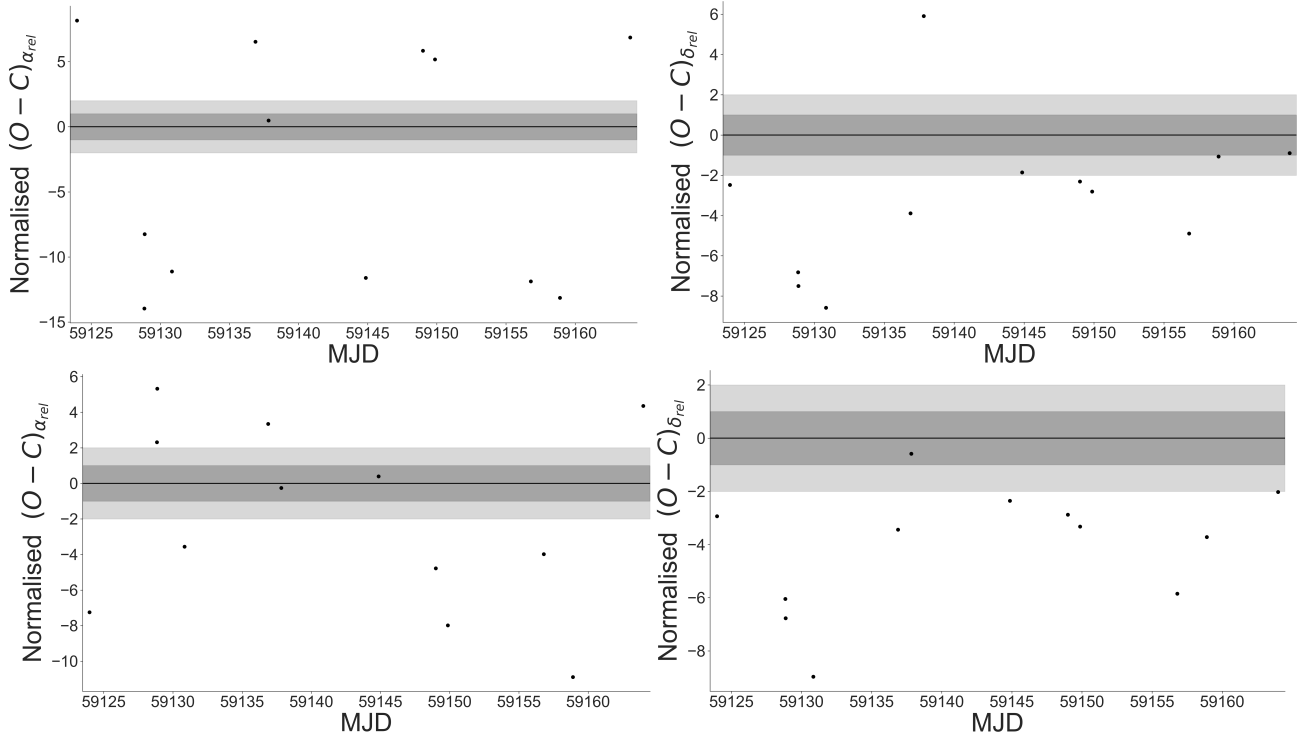


FIG. 6: Normalised residuals between observed and calculated data for each moon's relative position to Uranus. Oberon's data is on the top row and Titania's is on the bottom. Right ascension (α) and declination (δ) have been plotted separately. The dark and light shaded areas are one and two standard deviations away from the zero line respectively.

In figure 6 the right ascension residuals are randomly distributed above and below the zero line, but the declination residuals are disproportionately below the zero line. This suggests that there is a systematic error in the declination data for both moons. The telescopes used are very unlikely to be at fault since the images did not get calibrated using the telescope data. In addition, two different telescopes were used and it seems unreasonable that they would both have the same systematic error. It appears that the systematic error comes from the image analysis but this is unlikely since the images were calibrated with the Gaia catalogue and compared with JPL's latest ephemeris calculations, both of which are very accurate and precise. The only explanation is very unlikely: that this distribution of residuals is mere coincidence and that more data points might make it more reasonable. This is only supported by the fact that the lowest declination residuals ($\sim -8\sigma$) are within the range of the more reasonable right ascension residuals.

B. Projection of Orbits on the Sky

Chi-squared optimisation was used to fit ellipses to the moon's relative positions around Uranus as seen on the sky. The ellipse function had 5 fitting parameters which could be varied to match the moons' orbit (details given in section VII). Since there were twelve observations, this meant that there were 7 degrees of freedom. The fitting parameters were: the semi-major and semi-minor axes of the elliptical projection of the orbit on the sky (a and b respectively); the rotation angle of the ellipse (ϕ) measured anticlockwise from west direction in the sky; and the centre of the ellipse ((x_0, y_0)). The ellipse function was of the form $r(\theta)$ such that the observations could be fitted by minimising the radial distance to the ellipse. The radial distance was chosen over minimising x or y

distance to the ellipse because if a data point was above or below a trial ellipse then it would have an undefined distance to the ellipse in the x direction (and similarly for the y direction if a data point was to the left or right of the ellipse) meaning that the chi-squared value would be undefined. The Cartesian data was transformed into polar co-ordinates using the method described in section VI.

Titania and Oberon are thought to have very low eccentricities [26], i.e. their orbits around Uranus are very circular. Since Uranus is many times more massive than either moon, we expect their barycentres to be very close to the centre of the planet i.e. Uranus is in the centre of the moons' orbits. The projection of this orbit on the sky should therefore be an ellipse with Uranus at the centre. The ephemeris data was fitted first to establish sensible values for 'perfect' data which could then be compared with the real observations. Also, the fitted ellipses for the ephemeris data acted as sensible initial ellipses for the real observations. The real data had errors ranging between $0.8'' < \alpha_r < 0.12''$. To match this, the ephemeris data was fitted using errors of $\alpha_r = 0.1''$. The fitted ephemeris data is shown in figure 7 and the real data in figure 9.

The ellipses fitted the ephemeris data well and converged to the points even when the initial ellipses were very different to the final fitted ellipses. This gave credence to this method and was used successfully on the real observations also. The radial residuals show that the ellipses are good fits to the data for both Oberon and Titania. For both moons, there are approximately half as many points inside and outside the ellipse and there is no obvious pattern in them. As discussed earlier, it is likely that the errors have been underestimated so it is reasonable that the residuals aren't within 1σ . Despite this, almost all of the residuals

	Observed		Calculated	
	Oberon	Titania	Oberon	Titania
χ^2_ν	9.1	7.7	3.6	1.5
$a(^{\circ})$	42.5 ± 0.1	31.7 ± 0.1	42.7 ± 0.1	32.0 ± 0.1
$b(^{\circ})$	33.0 ± 0.1	24.5 ± 0.1	33.98 ± 0.05	25.3 ± 0.1
$x_0(^{\circ})$	-0.3 ± 0.1	-0.4 ± 0.1	0.12 ± 0.05	0.1 ± 0.1
$y_0(^{\circ})$	-0.3 ± 0.1	-0.1 ± 0.1	-0.0 ± 0.1	0.1 ± 0.1

TABLE IV: The optimised parameters for the ellipses fitted to the orbits of the moons projected onto the sky.

are within 2σ which suggests that the ellipse is a good fit regardless.

The key results of the chi-squared optimisations are shown in table IV. The errors of the parameters have been estimated by taking the square root of the diagonal elements of the covariance matrix obtained from the chi-squared optimisation. The parameters for the observations' ellipse are in reasonable agreement with those from the ephemeris' ellipse since they are almost all within $2-3\sigma$ of each other. Additionally, we have confirmed that Uranus is at the centre of their orbits since the centres of the ellipses are almost all in reasonable agreement with 0. There is further evidence that the errors have been underestimated. The expected value of reduced chi-squared value is $\chi^2_\nu = 1$. If the errors are too small then the reduced chi-squared value will be overestimated since the chi-squared statistic will be overestimated for each data point. We see this when fitting to the theoretical ephemeris data using comparable errors. The reduced chi-squared values are slightly too large: 3.6 and 1.5 respectively. With more reasonable errors we would see a reduction in all the reduced chi-squared values but it is impossible to know by how much. This puts the real values of 9.1 and 7.7 into some perspective, however they still seem much larger than the calculated values. The systematic error in declination identified earlier can be seen slightly since the values of y_0 for the observed values are significantly lower than those for the ephemeris. There are many values of rotation angle (ϕ) that result in the same ellipse so it is meaningless to draw comparisons using it. As a result it has been omitted from the table.

C. Recovering Periods

Chi-squared optimisation was also used to fit sinusoidal waves to each moon's movement in the right ascension and declination directions individually. The function used for fitting was:

$$y = A \sin\left(\frac{2\pi}{T}t - b\right) + c \quad (5)$$

Where y is the co-ordinate in question (right ascension or declination), t is the time in MJD, A is the amplitude of the wave and b & c are x and y translations respectively. As before, since the moon is orbiting around Uranus at the origin we expect $c=0$. The most important parameter is the period (T) in days since this is the period of each moon's real orbit around Uranus. There are 4 fitting parameters so there are 8 degrees of freedom. Figure 8 shows the ephemeris data and figure 10 shows the observed data. The ephemeris data

was fitted with reasonable errors of $\alpha=0.1''$ and showed that the curves fitted the data reasonably even when the initial and final curves were very different. This meant the fitted curves could be used as initial guesses for the real observations. The residuals for the real data show no patterns and are within 2σ of the fitted curve with few exceptions, implying that the sinusoidal curve is a reasonable fit for this data. As before, the residuals may be improved to be within 1σ of the curve if the errors weren't underestimated.

The optimised chi-squared parameters are shown in tables V and VI for Oberon and Titania respectively. Instead of calculating errors using the covariance matrix, jackknife resampling was used in order to get the most accurate values for the errors. The jackknife method calculates a parameter without one particular data point and then repeats this for every data point. The mean and standard error of these calculated parameters can then be used to estimate the true value and standard error. The jackknife method is useful in regimes where the number of data points is a limiting factor. In this case, chi-squared optimisation was performed on the ephemeris and real datasets (with one data point removed each time) and the values for T , A and c were recorded. This resulted in very precise parameters for the real observations but less precise parameters for the ephemeris data. This suggests that the fitted curves varied more in the ephemeris data when one point is removed compared to the real data. The period data both Oberon and Titania agree excellently with the ephemeris data and agree reasonably with the literature values of 13.46 and 8.706 days respectively [26]. The amplitudes and y translations appear to in disagreement and the y translations are not close to 0, this could be explained by the systematic error in declination identified earlier. However, there was no systematic error in right ascension and their y translations are also not close to 0 so this may be caused by the underestimation of errors. The reduced chi-squared values follow a similar pattern to the orbital data and have been affected by the underestimation of errors. Many identical curves can have the same value of x translation, it is therefore meaningless to compare its values between data sets so it has been omitted.

	Observed		Calculated	
	α_{rel}	δ_{rel}	α_{rel}	δ_{rel}
χ^2_ν	8.3	10.7	3.5	1.9
$T(\text{days})$	13.470 ± 0.001	13.470 ± 0.001	13.69 ± 0.09	13.68 ± 0.09
$A(^{\circ})$	33.09 ± 0.01	42.50 ± 0.02	36.63 ± 0.01	42.23 ± 0.01
$c(^{\circ})$	-0.59 ± 0.01	-0.34 ± 0.01	-0.61 ± 0.03	-0.21 ± 0.01

TABLE V: The optimised parameters for the sinusoidal curves fitted to Oberon.

	Observed		Calculated	
	α_{rel}	δ_{rel}	α_{rel}	δ_{rel}
χ^2_ν	6.1	7.1	2.0	1.38
$T(\text{days})$	8.703 ± 0.001	8.703 ± 0.001	8.7 ± 0.3	8.9 ± 0.3
$A(^{\circ})$	24.94 ± 0.01	31.69 ± 0.01	25.01 ± 0.02	31.56 ± 0.01
$c(^{\circ})$	-0.33 ± 0.01	-0.24 ± 0.01	-0.0 ± 0.1	0.00 ± 0.03

TABLE VI: The optimised parameters for the sinusoidal curves fitted to Titania.

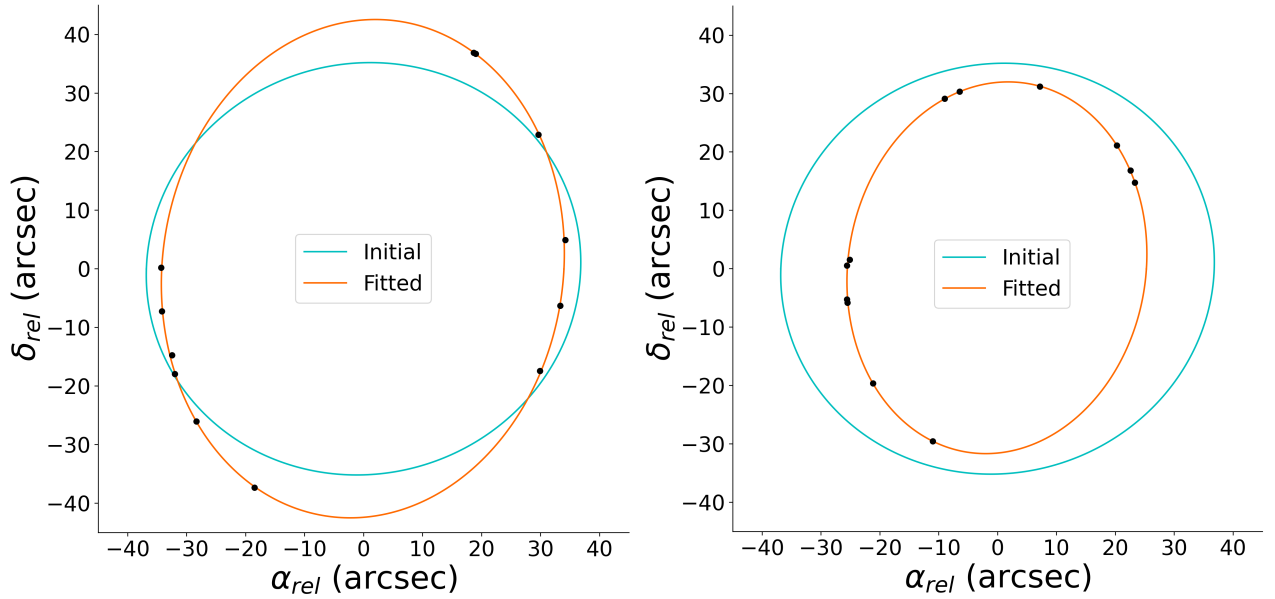


FIG. 7: Predicted orbits of Oberon (left) and Titania (right) relative to Uranus' position at the origin. Elliptical orbits fitted with chi-squared optimisation are shown in orange, the initial guessed orbits are shown in cyan.

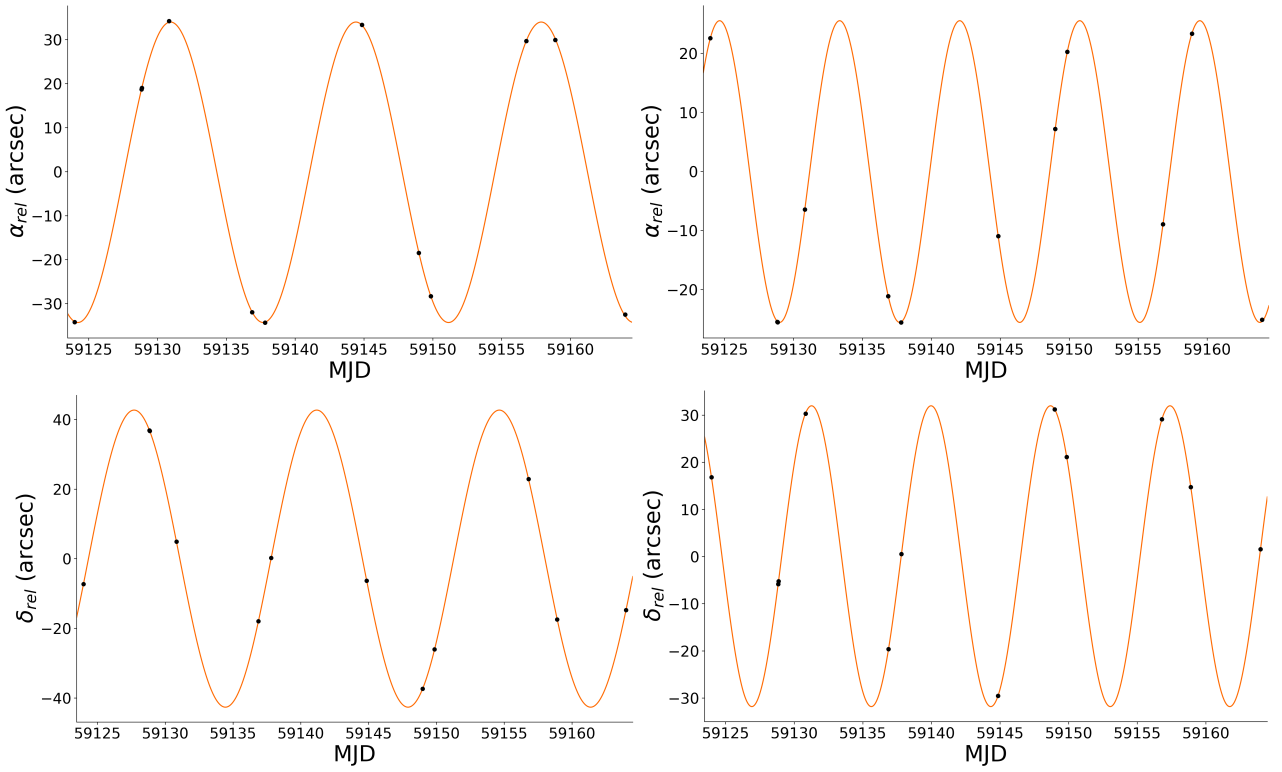


FIG. 8: Predicted movement of Oberon (left) and Titania (right) in the right ascension (top) and declination (bottom) directions respectively. Sinusoidal curves have been fitted using chi-squared optimisation as shown in orange. The initial guessed curves have been omitted for clarity.

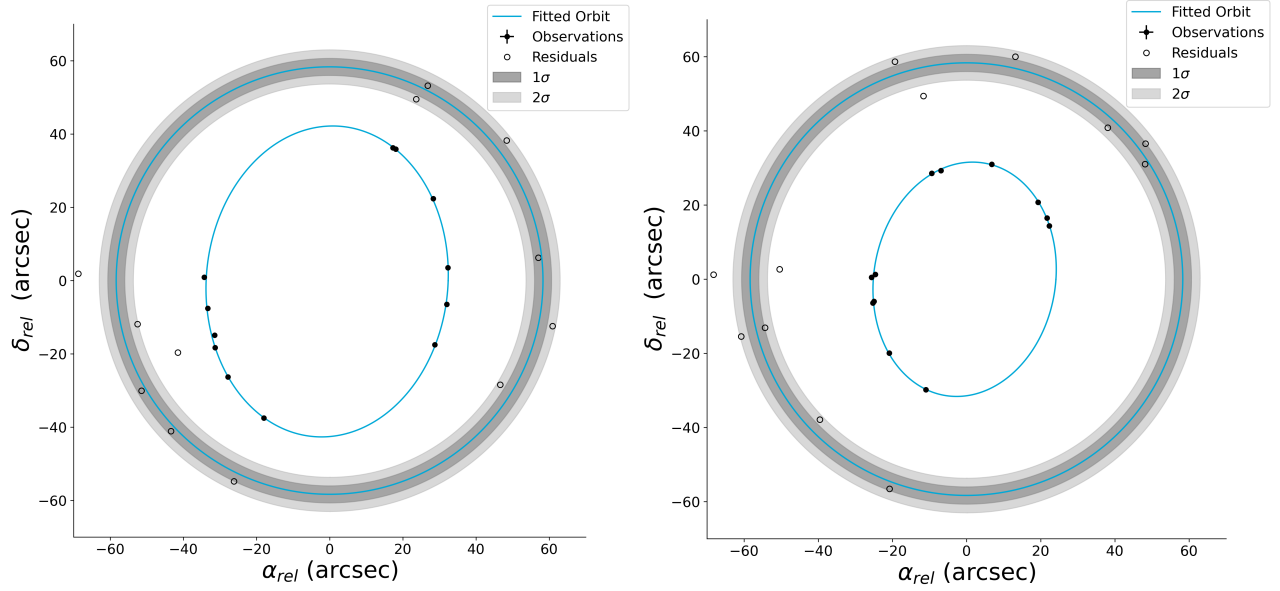


FIG. 9: Observed orbits of Oberon(left) and Titania (right) relative to Uranus' position at the origin. Elliptical orbits fitted with chi-squared optimisation are shown in blue. Error bars are too small to be seen in the observations. Normalised residuals between the observations and the fitted orbit have been plotted radially as black rings. The dark and light shaded areas are one and two standard deviations away from the fitted orbit respectively.

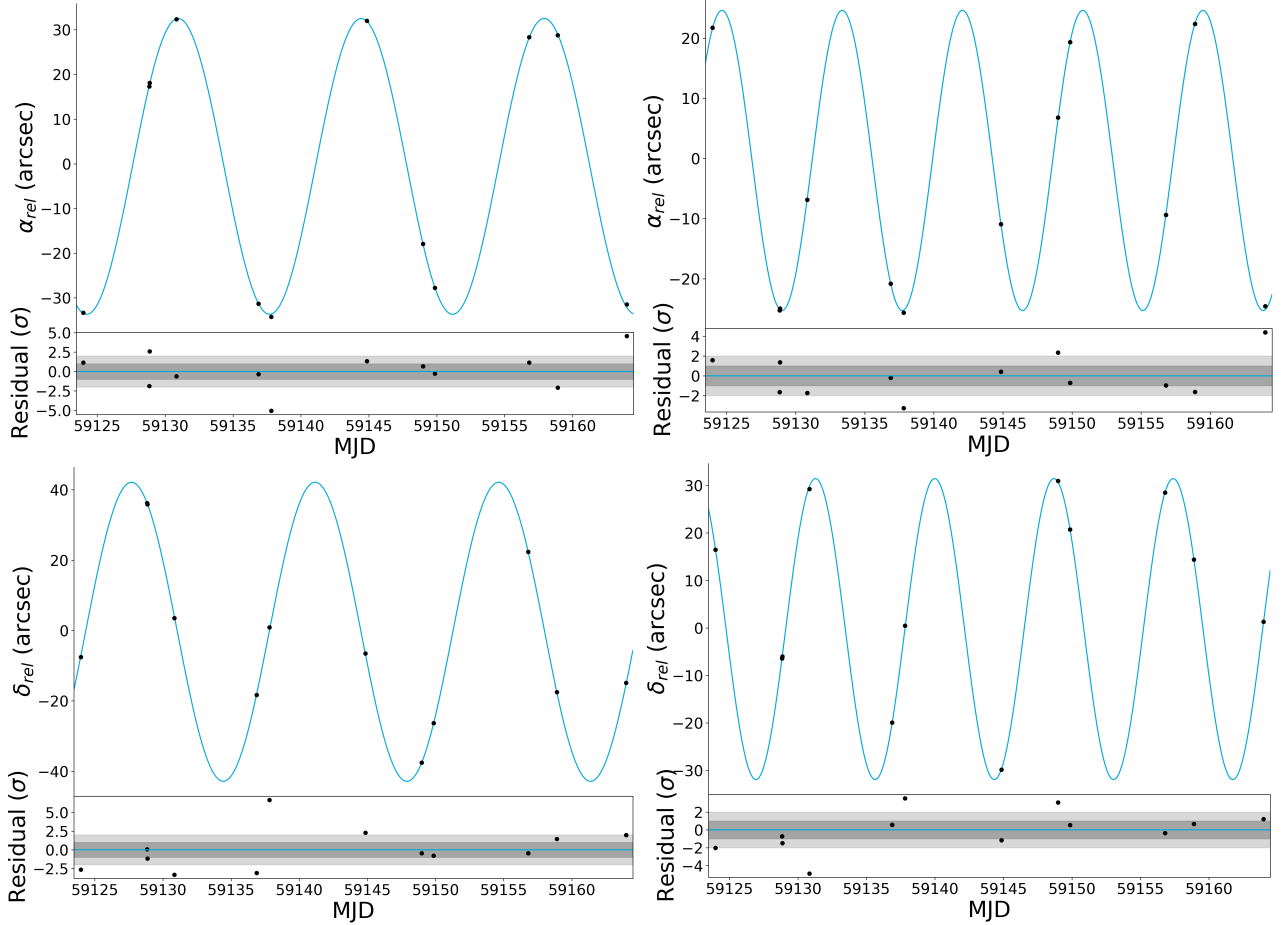


FIG. 10: Observed movement of Oberon (left) and Titania (right) in the right ascension (top) and declination (bottom) directions respectively. Sinusoidal curves have been fitted using chi-squared optimisation as shown in blue. Error bars are too small to be seen in the observations. Normalised residuals between the observations and the fitted curve are plotted below. The dark and light shaded areas are one and two standard deviations away from the fitted orbit respectively.

IV Conclusion

Twelve observations of Oberon and Titania taken at Durham University using 14" and 16" telescopes in October and November 2020 have been presented. They were analysed using GAIA and DS9 software to calculate their relative positions to Uranus. The images were calibrated by comparing background stars to the Gaia catalogue of known stars. They were compared to NASA's DE441 ephemeris and the data was found to be within 2" of each other. By analysing the residuals a systematic error in declination was identified and it was discovered that the method of determining the centre of Uranus underestimated the uncertainties. By plotting the projection of the orbits of the moons it was confirmed that Uranus is in the centre of the moons' orbits. By plotting the moon's motion in the right ascension and declination directions individually their periods were determined as 13.470 ± 0.001 and 8.703 ± 0.001 days for Oberon and Titania respectively.

The work of this report can be improved and extended by taking shorter exposures of only Uranus between the longer exposures of the moons in order to more accurately determine uncertainties in the centre of the planet. In some frames, the inner moons of Uranus could be seen. However these frames were rare and required very good seeing. If this work was continued for longer or was repeated with a more powerful telescope, it may be possible to analyse the inner moons as well. Continuing the project for longer would also extend the baseline of the data and increase the precision of the period calculations.

This report has shown that it is possible to perform astrometry on the moons of Uranus and reasonably recover their orbital parameters using telescopes with large FOVs and small apertures. If a probe does eventually visit the ice giants in the 2030s, it is necessary for more reports like this to have maintained accurate and precise ephemerides in order for the mission to be successful.

V Acknowledgements

The author would like to thank Professor Mark Swinbank and Professor Alastair Edge for their helpful advice, willingness to work late into the night for the benefit of students and their hard work in making sure the module ran smoothly despite the pandemic.

This work has used the Graphical Astronomy and Image Analysis tool (GAIA) [27] and SAOImage DS9 [28]. This work has used data from JPL's DE441 ephemeris [22].

This work has made use of data from the European Space Agency (ESA) mission *Gaia* (<https://www.cosmos.esa.int/gaia>), processed by the *Gaia* Data Processing and Analysis Consortium (DPAC, <https://www.cosmos.esa.int/web/gaia/dpac/consortium>). Funding for the DPAC has been provided by national institutions, in particular the institutions participating in the *Gaia* Multilateral Agreement [29] [30].

References

- [1] Helled, R., Nettelmann, N. and Guillot, T., 2020. Uranus and Neptune: Origin, Evolution and Internal Structure. *Space Science Reviews*, 216(3).
- [2] Helled, R., Anderson, J. D., Podolak, M., & Schubert, G. (2010). Interior models of Uranus and Neptune. *Astrophys. J.* 726(1), 15.
- [3] Hofstadter, M., Simon, A., Reh, K., Elliot, J., Nieber, C. and Colangeli, L., 2017. Ice Giants Pre-Decadal Study Final Report. California: NASA.
- [4] Pollack, J., Hubickyj, O., Bodenheimer, P., Lissauer, J., Podolak, M. and Greenzweig, Y., 1996. Formation of the Giant Planets by Concurrent Accretion of Solids and Gas. *Icarus*, 124(1), pp.62-85.
- [5] Planets Beyond our Solar System. Exoplanet Exploration: Planets Beyond our Solar System. Available at: <https://exoplanets.nasa.gov/>.
- [6] Deleuil, M., Pollacco, D., Baruteau, C., Rauer, H. and Blanc, M., 2020. Observational Constraints on the Formation and Evolution of Neptune-Class Exoplanets. *Space Science Reviews*, 216(6).
- [7] Cavalie, T., Venot, O., Miguel, Y., Fletcher, L., Wurz, P., Mousis, O., Bounaceur, R., Hue, V., Leconte, J. and Dobrevic, M., 2020. The Deep Composition of Uranus and Neptune from In Situ Exploration and Thermochemical Modeling. *Space Science Reviews*, 216(4).
- [8] Simon, A., Fletcher, L., Arridge, C., Atkinson, D., Coustenis, A., Ferri, F., Hofstadter, M., Masters, A., Mousis, O., Reh, K., Turrini, D. and Witasse, O., 2020. A Review of the in Situ Probe Designs from Recent Ice Giant Mission Concept Studies. *Space Science Reviews*, 216(1).
- [9] Hofstadter, M., Simon, A., Reh, K., Elliot, J., Nieber, C. and Colangeli, L., 2017. Ice Giants Pre-Decadal Study Executive Summary. California: NASA.
- [10] Shen, K., Qiao, R., Harper, D., Hadjifotinou, K. and Liu, J., 2002. Astrometry of five major Uranian satellites in 1995–1997. *Astronomy & Astrophysics*, 391(2), pp.775-779.
- [11] Izmailov, I., Korotkii, S., Ereshko, M. and Stepura, A., 2007. Astrometric observations of the second, third, and fourth satellites of Uranus. *Solar System Research*, 41(1), pp.42-45.
- [12] Qiao, R., Cheng, X., Dourneau, G., Xi, X., Zhang, H., Tang, Z. and Shen, K., 2012. CCD astrometric observations of the five major Uranian satellites made in 1998–2007 and comparison with theory. *Monthly Notices of the Royal Astronomical Society*, 428(3), pp.2755-2764.
- [13] Veiga, C., Vieira Martins, R. and Andrei, A., 2003. Positions of Uranus and Its Main Satellites. *The Astronomical Journal*, 125(5), pp.2714-2720.
- [14] Xie, H., Peng, Q., Wang, N., Vienne, A., Li, C., Xie, M. and Liu, Z., 2019. New CCD astrometric observations of the five major uranian satellites using Gaia DR1 in 2014–2016. *Planetary and Space Science*, 165, pp.110-114.
- [15] Dement'eva, A., 2015. Astrometric CCD observations of the third and the fourth moons of Uranus with the normal astrograph at the Pulkovo observatory. *Solar System Research*, 49(5), pp.360-365.
- [16] Morgado, B., Assafin, M., Vieira-Martins, R., Camargo, J., Dias-Oliveira, A. and Gomes-Júnior, A., 2016. Astrometry of mutual approximations between natural satellites. Application to the Galilean moons. *Monthly Notices of the Royal Astronomical Society*, 460(4), pp.4086-4097.
- [17] Santos-Filho, S., Assafin, M., Morgado, B., Vieira-Martins, R., Camargo, J., Gomes-Júnior, A. and Benedetti-Rossi, G., 2019. Mutual approximations between the five main moons of Uranus. *Monthly Notices of the Royal Astronomical Society*, 490(3), pp.3464-3475.
- [18] Mallama, A., Sôma, M., Sada, P., Modic, R. and Ellington, C., 2009. Astrometry of Iapetus, Ariel, Umbriel, and Titania from eclipses and occultations. *Icarus*, 200(1), pp.265-270.

- [19] Miller, C. and Chanover, N., 2009. Resolving dynamic parameters of the August 2007 Titania and Ariel occultations by Umbriel. *Icarus*, 200(1), pp.343-346.
- [20] NASA, 1986. True Colour Image Of Uranus. [image] Available at: <https://voyager.jpl.nasa.gov/assets/images/galleries/images-voyager-took/uranus/1bg.jpg>.
- [21] Sorensen, P., Azzaro, M. and Méndez, J., 2002. Object Visibility. [online] Catserver.ing.iac.es. Available at: <http://catserver.ing.iac.es/staralt/index.php>.
- [22] Ssd.jpl.nasa.gov. 2020. HORIZONS Web-Interface. [online] Available at: <https://ssd.jpl.nasa.gov/horizons.cgi>.
- [23] Space.jpl.nasa.gov. 2020. NASA/JPL Solar System Simulator. [online] Available at: <https://space.jpl.nasa.gov/>.
- [24] Raab, H., 2003. Detecting and measuring faint point sources with a CCD. [online] Linz: Astronomical Society of Linz. Available at: <http://www.astrometrica.at/Papers/PointSources.pdf>; [Accessed 22 April 2021].
- [25] Park, R., Folkner, W., Williams, J. and Boggs, D., 2021. The JPL Planetary and Lunar Ephemerides DE440 and DE441. *The Astronomical Journal*, 161(3), p.105.
- [26] Laskar, J. and Jacobson, R.A. (1987) “GUST86. An analytical ephemeris of the Uranian satellites”, *Astronomy & Astrophysics* 188, 212
- [27] Draper, P., 2016. GAIA - Graphical Astronomy and Image Analysis Tool. [online] Star-dur.ac.uk. Available at: <http://star-www.dur.ac.uk/pdraper/gaia/gaia.html>; [Accessed 22 April 2021].
- [28] Joye, W. and Mandel, E., 2003. New Features of SAOImage DS9. [online] Cambridge MA: Astronomical Society of the Pacific, pp.489-492. Available at: <http://adsabs.harvard.edu/pdf/2003ASPC..295..489J>; [Accessed 22 April 2021].
- [29] Gaia Collaboration, A. G. A. Brown, A. Vallenari, T. Prusti, J. H. J. de Bruijne, F. Mignard, R. Drimmel, C. Babusiaux, C. A. L. Bailer-Jones, U. Bastian and et al. (2016a) Gaia Data Release 1. Summary of the astrometric, photometric, and survey properties. *A&A* 595, pp. A2.
- [30] Gaia Collaboration, T. Prusti, J. H. J. de Bruijne, A. G. A. Brown, A. Vallenari, C. Babusiaux, C. A. L. Bailer-Jones, U. Bastian, M. Biermann, D. W. Evans and et al. (2016b) The Gaia mission. *A&A* 595, pp. A1.
- [31] Hughes, I. and Hase, T., 2014. Measurements and their Uncertainties. Oxford: OUP Oxford.

VI Error Appendix

Error analysis performed using Measurements and their Uncertainties by Hughes and Hase [31]. Chi-squared optimisation was used to fit models to the data. In general, the chi-squared parameter is defined as:

$$\chi^2 = \sum_i \left(\frac{y_i - y(x_i)}{\alpha_i} \right)^2 \quad (6)$$

where x_i and y_i are the observed data points and $y(x_i)$ is the value of y predicted by the model function. The uncertainty in the y direction of point i is given by α_i .

When combining errors in x (right ascension) and y (declination) directions to get radial errors, the error propagation was performed using the functional approach i.e. finding the contribution to the error from each coordinate and adding them in quadrature. Using the standard definition for radial distance:

$$r^2 = x^2 + y^2 \Rightarrow r(x, y) = \sqrt{x^2 + y^2} \quad (7)$$

We can define the error contribution in r from the x and y directions respectively as:

$$\begin{aligned} \alpha_r^x &= |r(x + \alpha_x, y) - r(x, y)| \\ &= |\sqrt{(x + \alpha_x)^2 + y^2} - \sqrt{x^2 + y^2}| \end{aligned} \quad (8)$$

$$\begin{aligned} \alpha_r^y &= |r(x, y + \alpha_y) - r(x, y)| \\ &= |\sqrt{x^2 + (y + \alpha_y)^2} - \sqrt{x^2 + y^2}| \end{aligned} \quad (9)$$

to get the final error in r as:

$$\alpha_r^2 = \alpha_x^2 + \alpha_y^2 \quad (10)$$

Note that for clarity x and y have been used for right ascension and declination instead of α and δ to avoid confusion with the standard error α . This functional method of combining multi-variable errors was also used to find the relative positions of the moons(\mathfrak{C}) with respect to Uranus (\mathfrak{U}) except equation 7 was replaced with:

$$\begin{pmatrix} x_{\text{rel}} \\ y_{\text{rel}} \end{pmatrix} = \begin{pmatrix} x_{\mathfrak{C}} \\ y_{\mathfrak{C}} \end{pmatrix} - \begin{pmatrix} x_{\mathfrak{U}} \\ y_{\mathfrak{U}} \end{pmatrix} \quad (11)$$

VII Ellipse Derivation Appendix

A particular equation of an ellipse needed to be derived with specific requirements in order to be used in chi-squared optimisation:

- To fit an ellipse using chi-squared, it needs to be of the form $f(x)$, in particular since the observations were being fitted radially it needed to be of the form $r(\theta)$.
- The ellipse needed to have enough parameters to both freely rotate and translate in the plane of the sky to fit the observations.
- The angle of rotation (ϕ), axes scales in x and y direction (a and b respectively) and the centre of the ellipse (x_0, y_0) needed to be defined explicitly so that the chi-squared code could easily vary them.

It is known that the moons orbit in ellipses and not hyperbolas or parabolas, so the general equation of a conic section could not be used. This meant a new equation for an ellipse was needed; using a combination of Cartesian co-ordinates for the translation of the centre of the ellipse and polar co-ordinates for the rotation. We begin with the cartesian equation of an ellipse that has been translated to a new centre (x_0, y_0):

$$\frac{(x - x_0)^2}{a^2} + \frac{(y - y_0)^2}{b^2} = 1 \quad (12)$$

To transform into polar co-ordinates we apply the standard substitutions $x = r \cos \psi$ and $y = r \sin \psi$ to equation 12. For brevity, we have defined $\psi = \theta - \phi$ (i.e. rotating by angle ϕ) although in the chi-squared program ϕ was left explicitly in the equation.

$$\frac{(r \cos \psi - x_0)^2}{a^2} + \frac{(r \sin \psi - y_0)^2}{b^2} = 1 \quad (13)$$

Expanding this equation and solving for r eventually leads to:

$$r = \frac{b^2 x_0 \cos \psi + a^2 y_0 \sin \psi \pm ab \sqrt{x_0 y_0 \sin(2\psi) + (b^2 - y_0^2) \cos^2 \psi + (a^2 - x_0^2) \sin^2 \psi}}{b^2 \cos^2 \psi + a^2 \sin^2 \psi} \quad (14)$$

Note that before the ellipse is rotated, the axes scales (a and b) are the semi-major and semi-minor axes (depending on which is biggest). Note also that once the ellipse has been rotated, the axes scales can swap. For example when rotating by $\pi/2$ the x axis scale (a) may actually be the y axis scale or when rotating by a non-multiple of $\pi/2$, a and b aren't tied to any axes at all. This is not a problem for the computer but can be confusing to refer to in text. For clarity, in this report a is always presented as the semi-major axis and b is always the semi-minor axis regardless of rotation.